



Binary chemical interaction and nonlinearity radiative flux of Williamson fluidic flow through Riga plate

Kotha Gangadhar, T. Sujana Sree & Ali J. Chamkha

To cite this article: Kotha Gangadhar, T. Sujana Sree & Ali J. Chamkha (18 Feb 2024): Binary chemical interaction and nonlinearity radiative flux of Williamson fluidic flow through Riga plate, International Journal of Modelling and Simulation, DOI: [10.1080/02286203.2024.2318753](https://doi.org/10.1080/02286203.2024.2318753)

To link to this article: <https://doi.org/10.1080/02286203.2024.2318753>



Published online: 18 Feb 2024.



Submit your article to this journal [↗](#)



Article views: 22






View related articles [↗](#)



View Crossmark data [↗](#)



Binary chemical interaction and nonlinearity radiative flux of Williamson fluidic flow through Riga plate

Kotha Gangadhar ^a, T. Sujana Sree ^b and Ali J. Chamkha ^c

^aDepartment of Mathematics, Acharya Nagarjuna University, Guntur, Andhra Pradesh, India; ^bR.V.R. & J.C. College of Engineering, Guntur;

^cFaculty of Engineering, Kuwait College of Science and Technology, Doha District, Kuwait

ABSTRACT

This Riga plate, which extends the configuration with permanent magnets and electrodes, may induce a wall-parallel Lorentz force over the magnetic field and exterior electric fields, enabling efficient control of the fluid flow. In this paper, the focus is on considering the three-dimensional flow characteristics of Williamson fluid past the Riga plate in the absence of variable thermal properties. Many influential factors, such as convective boundary conditions of temperature, viscous dissipation, binary chemical reactions, and thermal radiation, are studied in their analysis. To address the study problem, dimensionless parameters are used to clarify the conductive partial differential equations. This dimensionless form was consequently determined mathematically by applying the shooting technique. The affected engineering parameters were interpreted graphically to appeal to physical interest. It was observed that the velocity distribution slows down into the viscosity parameter and stretching ratio constant. The enhanced temperature distribution was noticed in the increase in the thermal conductivity parameter. The rate of heat transport (130.56%) rises in the presence of Biot numbers. This causes significant increases in convective heat transport and heat energy.

ARTICLE HISTORY

Received 17 October 2023

Accepted 11 February 2024

KEYWORDS

Binary chemical reaction;
convective transport;
thermal radiation; riga plate;
viscous dissipation

1. Introduction

This Riga plate, calm on changing permanent magnets and electrodes, had appeared by the assuring electromagnetic actuators into important potential by different functions. Its effectiveness in decreasing skin friction, reassuring boundary layer separation, and reducing pressure drag in submersibles had been established. The magnetic force-drive flows over this Riga plate show the critical effect on various industrial and engineering processes, like reactor design by thermal nuclear reactors, MHD generators, and flow meters. The utilisations expand to food processing, civil engineering, mechanical engineering, chemical engineering, and biomechanics. Considerable analysis had been conducted to analyse the fluid properties of the laminar flow discussed about the Riga plate by the distance of physical features. Lielausis and Gailitis [1] depicted an innovative Riga plate by this electromagnetic actuator with a scaled permanent magnet and extensive electrodes, decreasing turbulence effects and efficiently preventing boundary layer separations. This Grinbergs term [2], exhibiting this wall-parallel Lorentz force into the decoupled momentum equations, totally means that the flow and reduce exponential in the direction is perpendicular to this plate. Asogwa et al. [3] studied the convective EMHD flow on

the water-placed nanofluids over the parabolic Riga plate. Ali and Jubair [4] have examined the ternary nanofluid flow on motile microbes through the Riga plate. Kayikci et al. [5] formulated that effect on thermally radiative flow and thermal stratification for the carbon nanotubes in the Riga plate to heat generations.

These fluids are classified into two kinds based on how shear stress affects them and how we act in Newtonian fluids and non-Newtonian fluids. The non-Newtonian fluids had different categories. Few of them, like quasi-plastics and suspensions, decline their basic concentrations into raising stress levels, although others, like that, display high resistance to rising stress levels as dilatants. Anyhow, this action in the non-Newtonian fluids did not build upon solely stress, which means that materials did not act orderly to sustain their strain rate and can be lazy or advance in time. This surprising performance led to a wider range of functions for these fluids in different areas of industry and engineering. In correlation with Newtonian fluids, non-Newtonian fluids are highly complex and pose numerical challenges. Presented that challenge, many researchers had made important contributions to non-Newtonian hydrodynamics studies [6–8]. This Williamson fluid had a viscous-

inelastic profile along the typical rheological profile; it can be well analysed based on the flow hypotheses and diverse abounding shapes. The effect of cross-diffusion impacts by the act on Dufour and Soret impacts inside the contexts by the flow in Casson fluids and two-dimensional Williamson through the stretched sheet to differing thickness is inspected as Sharma et al. [9]. Patil et al. [10] have done extensive analysis of the mass and heat transport in the MHD Williamson nanofluid flow past the permeable elongating surface along the chemical reaction. Their study concluded that the temperature profile was improved by the radiation impact. Nazeer et al. [11] derived a perturbation solution of multiphase flow on the non-Newtonian fluid passing over the steep medium.

The thermal conductance and viscosity, which were physical characteristics of the fluids, could not be covered by constants in industrial processes and engineering at higher temperatures because heat transmission was improved by drop-in fluid viscosity. Therefore, this rate of heat transmission and thermal boundary layer had necessary effects. In this instance, the effect on changes in thermal conductivity and viscosity models must be analysed by best prediction. Therefore, although studying transport phenomena, it was acquired into detail in viscosity alters for incompressible flows [12]. Akolade et al. [13] formulated the Powell-Eyring fluid past a three-dimensional Riga plate with microorganisms. Chaurasiya et al. [14] conducted the analysis on the one-phase affecting that boundary problem into the size-dependent thermal conductivities and affecting phase change materials. Vaidya et al. [15] scrutinised the peristaltic blood flow in Carreau fluid along with variable material characteristics. Ramzan et al. [16] studied the chemically reactive Maxwell nanofluid flow on a permeable medium to generalise Fick's and Fourier laws in the absence of temperature-dependent thermal conductivity in Robin conditions past the spinning cone. Vijay and Sharma [17] established the numerical solutions for thermal radiative incompressible flow by the hybrid nanofluid discussed for the radially stretched circulating disc in their entropy generation study. Ejaz and Mustafa [18] had a discussion about the unsteady flow across the slow-down circulating disc due to variable physical properties. Kumawat et al. [19] modelled the study of entropy generation by this MHD blood flow over the porous arched channel into a heat source and chemical reaction. Hussain and Farooq [20] explored the blood flow by the peristaltic esophageal artery, which contains migratory gyrotactic microorganisms and nanomaterials.

This analysis of heat transfer study shows that dissipation affects energy sources. Although this plate was cooling or heating, the values of joule heating and viscous dissipation were highly important. This notable case of heat transfer normally increases with the existence of cooling in electronic chips or metallic sheets, cooling in nuclear reactors, power generation systems, and liquid metal fluids. Considering all these aspects, Aziz et al. [21] reported the entropy generation of the radiative flow on nanoliquid with a rotating frame and activation energy. Bhatti et al. [22] recorded the entropy generation of hybrid nanoparticles under the effects of magnetic fields and viscous dissipation. Naseem and Shahzad [23] considered the shape influence on TiO_2 and Cu nanoparticles of the heat transport improvement past the radiated stretching sheet. Gangadhar et al. [24] discussed the radiation impact on the wall jet blood flow over the affecting surfaces. This transverse flow on the oxytactic microorganisms held by the motion of the Lorentz force past the porous Riga surface is analysed by Mahmud et al. [25]. The mixed convective Burgers nanofluids flow into generalising Fick's and Fourier's laws, which are explored by Juhany et al. [26]. Farooq et al. [27] considered mixed slip boundary conditions and nonlinear stratification on squeezed viscous fluid flow along viscous dissipation.

This phenomenon on radiative heat transport was significant regarding tremendous functions like combustion functions, power generation, and nuclear reactor cooling. This suitable acceptance mechanism for solar radiation had main significance for the modelled behaviour of developed energy conversion systems at greater temperatures. Examples of this fossil fuel combustion energy, systems, and solar power technology include astrophysical flows and space vehicle re-entry. This generally happened when the variation between surface and ambient temperatures was greater. Shafiq et al. [28] considered thermal radiation and convective boundary conditions on ethylene glycol-based nanofluid. Shoaib et al. [29] reported the theoretical calculations for the temperature gradient of 3D steady Casson fluid and activation energy during chemical reactions over an oscillating disk. He et al. [30] investigated the unsteady compressed magneto-radiative gas flow near a heated vertical wave wall in porous media. Fang et al. [31] described the impact on thermal radiations into the large incident angles and alone polarization. Padma Devi and Srinivas [32] concentrated on the combined effects of heat source and chemical reaction for heat and mass characteristics in the vertical porous medium filled into the two-layer viscoelastic liquid by the effect on the oscillating pressure gradient. Mahabaleshwar et al. [33] studied the unstable motion of the Newtonian fluid past

the stagnation point by the stretched sheet in the permeable channel. More studies are in Refs [34–52].

The analysis aims to contribute to the existing body of knowledge to address many gaps and provide novel awareness. Particularly, the novelty lies in the study of three-dimensional flow on the Williamson fluid by the Riga plate under the impact of binary chemical reactions. Furthermore, the impact of convective boundary conditions, nonlinearity, viscous dissipation, and thermal radiation on the temperature were examined. This analysis starts by studying the model and identifying the appropriate physical property connected to the problem. This effect on the many physical parameters was further depicted in the graphs. These solutions for surface physical quantities like heat transport rate and skin friction coefficient by different parameters were graphically given by applying bar charts. To consider that aspect, this analysis gives a comprehensive understanding of flow performance and connected physical quantity.

2. Physical model declaration

This numerical imitation by flowing movement of the magneto Williamson fluid near the side of the steady three-dimensional Riga plate was advanced. This analysis incorporates the effect of heat transport rate, viscous dissipation, convective condition, and thermal radiation of temperature. As illustrate in Figure 1, reactive movement and radiative were assumed for this Riga plate along the magnetic induction $M = M_0 x_0$ stationed by $z_0 = 0$, by constant wall concentricity C_w and fixed surface temperature T_f , as well as free streaming heat and concentration T_∞, C_∞ , respectively. This velocity on the

stretched Riga plate with y_0 - axes as $v_0 = b_0 y_0 = V_0$ and speed on the stretching Riga surface nearby x_0 - axes as $u_0 = a_0 x_0 = U_0$.

The advanced assumptions, as proposed by Srinivas et al. [], consider the rheological form of the Williamson fluid, leading to the Cauchy stress tensors as follows:

$$S_0 = -PI + \tau_w, \text{ where} \\ \tau_w = \left(\mu_\infty + \frac{\mu_0 - \mu_\infty}{1 - \Gamma_0 B_1} \right) S_1 \text{ and } B_1 = \sqrt{\frac{1}{2}} \pi \quad (1)$$

where S_0 signify the additional stress tensor, μ_∞ and μ_0 as the infinite shear rate and restrictive viscidness is zero, S_1 represents first Rivlin-Erickson tensor, $\Gamma_0 > 0$ shows that fixed time and $\pi = \text{trace}(S_1^2) = \text{trace}(V + (V)^T)^2$.

Supposition $\Gamma_0 B_1 < 1$ and $\mu_0 = 0$, τ_w as simplified into the under model by binomial extension

$$\tau_w = \left(\frac{\mu_0}{1 - \Gamma_0 B_1} \right) S_1 \Rightarrow \tau_w = \mu_0 (1 + \Gamma_0 B_1) S_1 \quad (2)$$

These produced equations for Srinivas et al. [36], Onwubuoya, and Dada [37] in the form of the help of the aforementioned premises.

$$\frac{\partial u_0}{\partial x_0} + \frac{\partial v_0}{\partial y_0} + \frac{\partial w_0}{\partial z_0} = 0, \quad (3)$$

$$\rho_0 \left(u_0 \frac{\partial u_0}{\partial x_0} + v_0 \frac{\partial u_0}{\partial y_0} + w_0 \frac{\partial u_0}{\partial z_0} \right) \\ = \frac{\partial}{\partial z_0} \left\{ \mu(T) \left[\frac{\partial u_0}{\partial z_0} + \frac{\Gamma_0}{\sqrt{2}} \left(\frac{\partial u_0}{\partial z_0} \right)^2 \right] \right\} + \frac{\pi j_0 M}{8} e^{-\frac{\pi}{\tau_0} z_0}, \quad (4)$$

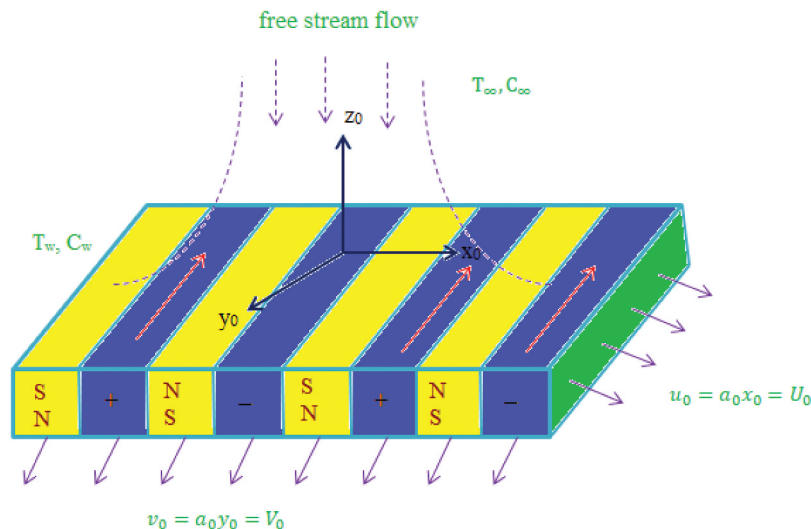


Figure 1. The physical model of the Williamson fluid flow over the Riga plate.

$$\begin{aligned} & \rho_0 \left(u_0 \frac{\partial v_0}{\partial x_0} + v_0 \frac{\partial v_0}{\partial y_0} + w_0 \frac{\partial v_0}{\partial z_0} \right) \\ &= \frac{\partial}{\partial z_0} \left\{ \mu(T) \left[\frac{\partial v_0}{\partial z_0} + \frac{\Gamma_0}{\sqrt{2}} \left(\frac{\partial v_0}{\partial z_0} \right)^2 \right] \right\}, \end{aligned} \quad (5)$$

$$\begin{aligned} & (\rho_0 C_p) \left(u_0 \frac{\partial T}{\partial x_0} + v_0 \frac{\partial T}{\partial y_0} + w_0 \frac{\partial T}{\partial z_0} \right) = \frac{\partial}{\partial z_0} \\ & \left\{ \kappa(T) \frac{\partial T}{\partial z_0} - q_r \right\} + \mu \left[\left(\frac{\partial u_0}{\partial z_0} \right)^2 + \left(\frac{\partial v_0}{\partial z_0} \right)^2 \right] \\ & + Q_0(T - T_\infty), \end{aligned} \quad (6)$$

$$u_0 \frac{\partial C}{\partial x_0} + v_0 \frac{\partial C}{\partial y_0} + w_0 \frac{\partial C}{\partial z_0} = D_0 \frac{\partial^2 C}{\partial z_0^2} - K_0(C - C_\infty)^n. \quad (7)$$

These conditions in the boundary were as follows:

$$u_0 = U_0, v_0 = V_0, w_0 = 0, T = T_w, C = C_w, by z_0 = 0, \quad (8)$$

$$u_0 \rightarrow 0, v_0 \rightarrow 0, w_0 = 0, T \rightarrow T_\infty, C \leftarrow C_\infty, by z_0 \rightarrow \infty. \quad (9)$$

where (u_0, v_0, w_0) are velocity components across (x_0, y_0, z_0) , C performs the concentricity, ρ symbolizes density, T denotes temperature, $\kappa(T)$ displays the varying temperature number, D_0 signifies the fixed mass diffusion, C_p as specific heat capacity, μ shows liquid viscidness, j_0 signifies the current density utilized into the electrode Q_0 by the heat source (sink) factor, r_0 represents the width in the magnets placed on the interval separate the electrodes and M_0 performs plate surface magnetostricture benefit in the permanent magnets. This total radiative heat on the support of temperature flowing the gradients regime (equation (6)) was simplified into adopting the Rosseland estimation by ([34]) $q_r = -\frac{4\sigma_c}{3k_c} \frac{\partial T^4}{\partial z_0} = -\frac{16\sigma_c}{3k_c} \frac{\partial}{\partial z_0} \left(T^3 \frac{\partial T}{\partial z_0} \right)$, where absorption factor k_c and Stefan-Boltzmann's constant σ_c were specified.

Indentation the following comparison transformations [35] and the temperature-based application by thermal conductance and dynamical viscidness was

$$\begin{aligned} u_0 &= a_0 x_0 \omega'(\xi), v_0 = a_0 y_0 g'(\xi), \\ w_0 &= -\sqrt{a_0 v} [\omega(\xi) + g(\xi)], \theta(\xi) = \frac{T - T_\infty}{T_f - T_\infty}, \\ \phi(\xi) &= \frac{C - C_\infty}{C_w - C_\infty}, \xi = z_0 \sqrt{\frac{a_0}{v}}, \\ \mu(T) &= \mu_0 [1 + m_1(T_w - T)], \kappa(T) = \kappa_0 [1 + m_2(T - T_\infty)]. \end{aligned} \quad (10)$$

Using beyond comparison conversions on the non-dimensional by the Eqs. (3–9), we have

$$\begin{aligned} & (1 + \lambda - \lambda\theta) [1 + We \omega''] \omega''' - \lambda \left(1 + \frac{1}{2} We \omega'' \right) \omega'' \theta' \\ & + Ha \exp(-\Lambda\xi) - \omega'^2 + (\omega + g) \omega'' = 0, \end{aligned} \quad (11)$$

$$\begin{aligned} & (1 + \lambda - \lambda\theta) [1 + We g''] g''' - \lambda \left(1 + \frac{1}{2} We g'' \right) g'' \theta' \\ & - g'^2 + (\omega + g) \omega'' = 0, \end{aligned} \quad (12)$$

$$\begin{aligned} & (1 + \gamma\theta) \theta'' + \gamma \theta'^2 + Rd [(1 + \delta_w \theta)^3 \theta']' + Pr(\omega + g) \theta' \\ & + Pr Q\theta + Pr Ec_1 \omega''^2 + Pr Ec_2 g''^2 = 0, \end{aligned} \quad (13)$$

$$\phi'' + Sc(\omega + g)\phi' - Sc Kr \phi^n = 0. \quad (14)$$

Converted borders constraints are

$$\begin{aligned} \omega(\xi) &= 0, \omega'(\xi) = 1, g(\xi) = 0, g'(\xi) = c, at \xi = 0, \\ \theta'(\xi) &= -Bi(1 - \theta(\xi)), \phi(\xi) = 1, \end{aligned} \quad (15)$$

$$\omega'(\xi) \rightarrow 0, g'(\xi) \rightarrow 0, \theta(\xi) \rightarrow 0, \Gamma(\xi) \rightarrow 0, as \xi \rightarrow \infty. \quad (16)$$

where $We = \sqrt{2}\Gamma U_0 \sqrt{\frac{a_0}{v}}$ stands for Williamson fluid term, $\lambda = m_1(T_f - T_\infty)$ denotes viscosity parameter, $\gamma = m_2(T_f - T_\infty)$ denotes thermal conductivity parameter, $Ha = \frac{\pi j_0 M_0}{8\rho_0 a_0^2}$ shows changed Hartmann number, $c = \frac{b_0}{a_0}$ displays stretching ratio, $\Lambda = \frac{\pi}{r_0} \sqrt{\frac{v}{a_0}}$ represent material constant combined into the magnetic surface electrode width, $Rd = \frac{16\sigma_c T_\infty^3}{k_c k}$ allocated as radiative term, $Pr = \frac{\rho_0 C_p v}{k}$ gives by Prandtl amount, $Q = \frac{Q_0}{a_0(\rho_0 C_p)}$ performs by heat generating or sink factor, $\delta_w = \frac{T_f - T_\infty}{T_\infty}$ labels as temperature difference

parameter, $Ec_1 = \frac{u_w^2}{C_p(T_f - T_\infty)}$ is Eckert number along x_0 - direction, $Ec_2 = \frac{v_w^2}{C_p(T_f - T_\infty)}$ is Eckert number along y_0 - direction, $Bi = \frac{h_f}{k} \sqrt{\frac{\nu}{a_0}}$ denotes the thermal Biot number, $Sc = \frac{\nu}{D_0}$ represents Schmidt amount, and $Kr = \frac{K_0}{a_0} (C_w - C_\infty)^{n-1}$ embodies as variable reaction factor.

Indentation initiated under was again on applicability into plans,

$$\begin{aligned} \tau_{wx_0} &= \left\{ \mu(T) \left[\frac{\partial u_0}{\partial z_0} + \frac{\Gamma}{\sqrt{2}} \left(\frac{\partial u_0}{\partial z_0} \right)^2 \right] \right\}_{z_0=0}, \\ \tau_{wy_0} &= \left\{ \mu(T) \left[\frac{\partial v_0}{\partial z_0} + \frac{\Gamma}{\sqrt{2}} \left(\frac{\partial v_0}{\partial z_0} \right)^2 \right] \right\}_{z_0=0}, \\ q_w &= \left\{ \kappa(T) \left[\frac{\partial T}{\partial z_0} + \frac{4\sigma_c}{3k_c} \frac{\partial T^4}{\partial z_0} \right] \right\}_{z_0=0}, \quad q_w = -D_0 \left(\frac{\partial C}{\partial z_0} \right)_{z_0=0}. \end{aligned} \quad (17)$$

The Sherwood number, Frictional force factors, and Nusselt number perform in the next terms:

$$\begin{aligned} C_{fx_0} &= \frac{\tau_{wx_0}}{\rho_0 a_0^2 x_0^2}, \quad C_{fy_0} = \frac{\tau_{wy_0}}{\rho_0 a_0^2 y_0^2}, \quad Nu_{x_0} \\ &= \frac{x_0 q_w}{k(T_f - T_\infty)}, \quad Sh_{x_0} = \frac{x_0 q_m}{D_0(C_w - C_\infty)}, \end{aligned} \quad (18)$$

and the dimensionless forms are

$$\sqrt{\text{Re}_{x_0}} C_{f_1} = [1 + \lambda - \lambda \theta(0)] \left(1 + \frac{1}{2} We \omega''(0) \right) \omega''(0), \quad (19)$$

$$\sqrt{\text{Re}_{y_0}} C_{f_2} = [1 + \lambda - \lambda \theta(0)] \left(1 + \frac{1}{2} We g''(0) \right) g''(0), \quad (20)$$

$$\frac{Nu_{x_0}}{\sqrt{\text{Re}_{x_0}}} = -[1 + \gamma \theta(0)] \{ 1 + Rd[1 + \delta_w \theta(0)]^3 \} \theta'(0), \quad (21)$$

$$\frac{Sh_{x_0}}{\sqrt{\text{Re}_{x_0}}} = -\phi'(0). \quad (22)$$

3. Numerical solution

Now, they assumed the numerical result the concerned with differential equations present in the shooting method. This molded Eqs. (10)-(14) was locally related and targeting applying the shooting technique (MATLAB software). Following these essential

processes, a set of equations is first transformed by first-order differential equations in the following ways:

$$\begin{aligned} \mathfrak{R}_1 &= \omega, \quad \mathfrak{R}_2 = \omega', \quad \mathfrak{R}_3 = \omega'', \quad \mathfrak{R}'_3 = \omega''', \quad \mathfrak{R}_4 = g, \\ \mathfrak{R}_5 &= g', \quad \mathfrak{R}_6 = g'', \quad \mathfrak{R}'_6 = g''', \quad \mathfrak{R}_7 = \theta, \quad \mathfrak{R}_8 = \theta', \\ \mathfrak{R}'_8 &= \theta'', \quad \mathfrak{R}_9 = \Gamma, \quad \mathfrak{R}_{10} = \Gamma', \quad \mathfrak{R}'_{10} = \Gamma'', \end{aligned} \quad (23)$$

$$\mathfrak{R}'_1 = \mathfrak{R}_2, \quad (24)$$

$$\mathfrak{R}'_2 = \mathfrak{R}_3, \quad (25)$$

$$\mathfrak{R}'_3 = \frac{1}{[1 + \lambda - \lambda \mathfrak{R}_7] \{ 1 + We \mathfrak{R}_3 \} \left[\lambda \left(1 + \frac{1}{2} We \mathfrak{R}_3 \right) \mathfrak{R}_3 \mathfrak{R}_8 - Ha e^{-\Lambda \xi} \right] + \mathfrak{R}_2^2 - (\mathfrak{R}_1 + \mathfrak{R}_4) \mathfrak{R}_3}, \quad (26)$$

$$\mathfrak{R}'_4 = \mathfrak{R}_5, \quad (27)$$

$$\mathfrak{R}'_5 = \mathfrak{R}_6, \quad (28)$$

$$\mathfrak{R}'_6 = \frac{1}{[1 + \lambda - \lambda \mathfrak{R}_7] \{ 1 + We \mathfrak{R}_6 \} \left[\lambda \left(1 + \frac{1}{2} We \mathfrak{R}_6 \right) \mathfrak{R}_6 \mathfrak{R}_8 + \mathfrak{R}_5^2 - (\mathfrak{R}_1 + \mathfrak{R}_4) \mathfrak{R}_6 \right]}, \quad (29)$$

$$\mathfrak{R}'_7 = \mathfrak{R}_8, \quad (30)$$

$$\mathfrak{R}'_8 = \frac{1}{1 + \gamma \mathfrak{R}_7 + Rd(1 + \delta_w \mathfrak{R}_7)^3 \left[\gamma \mathfrak{R}_8^2 + 3Rd(1 + \delta_w \mathfrak{R}_7)^2 \mathfrak{R}_8^2 + \text{Pr}(\mathfrak{R}_1 + \mathfrak{R}_4) \mathfrak{R}_8 \right] + \text{Pr} Q \mathfrak{R}_7 + \text{Pr} Ec_1 \mathfrak{R}_3^2 + \text{Pr} Ec_2 \mathfrak{R}_6^2}, \quad (31)$$

$$\mathfrak{R}'_9 = \mathfrak{R}_{10}, \quad (32)$$

$$\mathfrak{R}'_{10} = -Sc(\mathfrak{R}_1 + \mathfrak{R}_4) \mathfrak{R}_{10} + ScKr \mathfrak{R}_9^n, \quad (33)$$

The connected boundary conditions yield

$$\begin{aligned} \mathfrak{R}_1(0) &= 0, \quad \mathfrak{R}_2(0) = 1, \quad \mathfrak{R}_4(0) = 0, \quad \mathfrak{R}_5(0) = c, \quad \mathfrak{R}'_8(0) \\ &= -Bi(1 - \mathfrak{R}_7(0)), \quad \mathfrak{R}_9(0) = 1, \end{aligned} \quad (34)$$

$$\mathfrak{R}_2(\infty) = 0, \quad \mathfrak{R}_5(\infty) = 0, \quad \mathfrak{R}_7(\infty) = 0, \quad \mathfrak{R}_9(\infty) = 0. \quad (35)$$

Through iterative mathematical computations, a desirable level of accuracy with results up to 10^{-5} has been achieved.

Table 1. Correlation of $-\theta'(0)$ with change in the prandtl number, and all other parameters are absent.

Pr	Qureshi [35]	Shamshuddin et al. [34]	Present results
0.72	0.8087618	0.8087612	0.80883421
1.0	1.0000000	1.0000000	1.00000838
3.0	1.9235742	1.9235734	1.92367859
7.0	3.0731465	3.0731465	3.07224720
10.0	3.7205542	3.7205511	3.72067116

4. Code validation

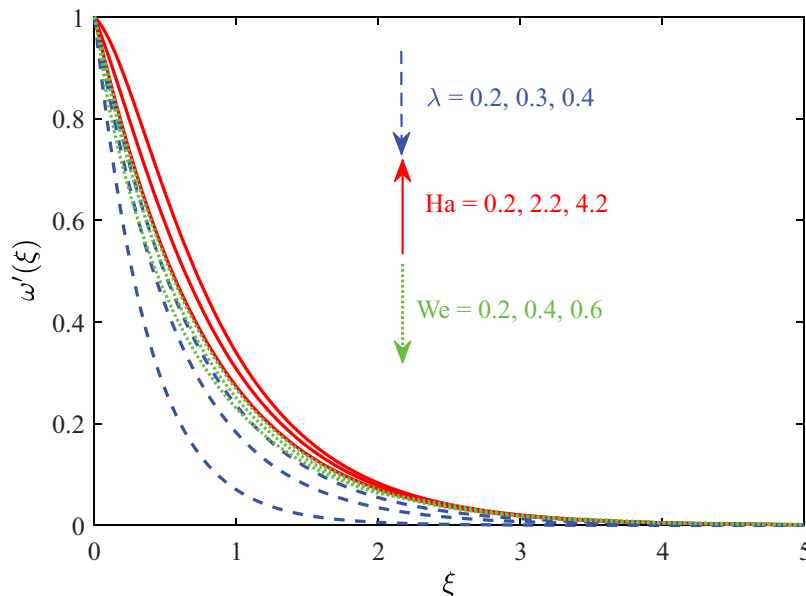
To confirm the effectiveness of the computational method in examining the heat transport rate, a comparison was made with the established findings from previous studies [34,35]. Table 1 illustrates the correlation between the outcomes of the current analysis and the solutions obtained in earlier investigations. The results of the present research were presented, demonstrating a high level of accuracy comparable to previous studies.

5. Results and discussion

In this analysis, the heat transport characteristics of the flow by Williamson fluid connected into the Riga surface had been recorded numerically. The acquired numerical values were given by temperature, velocity, and concentration profiles. The detailed graphical investigations of every parameter have been displayed into differing, although the remaining parameters' values were kept at a constant like that $\lambda = 0.1$, $We = 0.1$, $Ha = 0.3$, $\Lambda = 4.0$, $m\gamma = 0.2$, $Rd = 0.1$, $\delta_w = 1.5$, $Pr = 0.71$, $Q = 0.1$, $Sc = 0.62$, $Kr = 0.5$, $n = 2.0$, $Ec_1 = 0.1$, $Ec_2 = 0.1$, $Bi = 0.4$, $c = 0.6$.

Figures 2 and 3 illustrate the non-Newtonian Williamson liquid factor, Hartmann number, and viscosity parameter effect of the Williamson fluid velocities $\omega'(\xi)$, $g'(\xi)$. This Hartmann number characterized that the magnetic field effect generates the electromagnetic force to examine Non-Newtonian reactions. According to Figures 3(a, b), when the heat is dependent on thermos-dynamic Riga plate and viscosity it assured that major flow velocities, this boundary layers thicknesses velocities and electromagnetic actuator raised. To observe, that dragged impact on the material viscosity was dominated by that increasing the velocity. Anyhow, this secondary velocity in boundary layer thickness and the flow assured that fluid material viscosities, the solution on damp velocities profiles to observed. The more electromagnetic force was discussed for secondary Williamson fluid flows it conducts inter heating, as a result, decreasing the flow velocities on the fluids and the wall thickness velocity.

The results presented in Figures 1 and 3 demonstrate the impact of increasing the Non-Newtonian Williamson liquid factors on the primary and secondary velocities with the monotonically rising bounded region (ξ). In this modeling, the material shear is characterized by infinite fluid viscosity, causing the velocities shown in Figures 2 and 3 to exhibit damping effects due to the rising material term. Furthermore, in stress-controlled flow, the unregulated flows are suppressed within the reacting fluids. As a result of this reaction, the velocity profiles transition into infinite fluid streams. In Figures 2 and 3, the Williamson fluid viscosity term was analysed on the flow velocities dimension. Due to the

**Figure 2.** Velocity $\omega'(\xi)$ via λ , Ha and We .

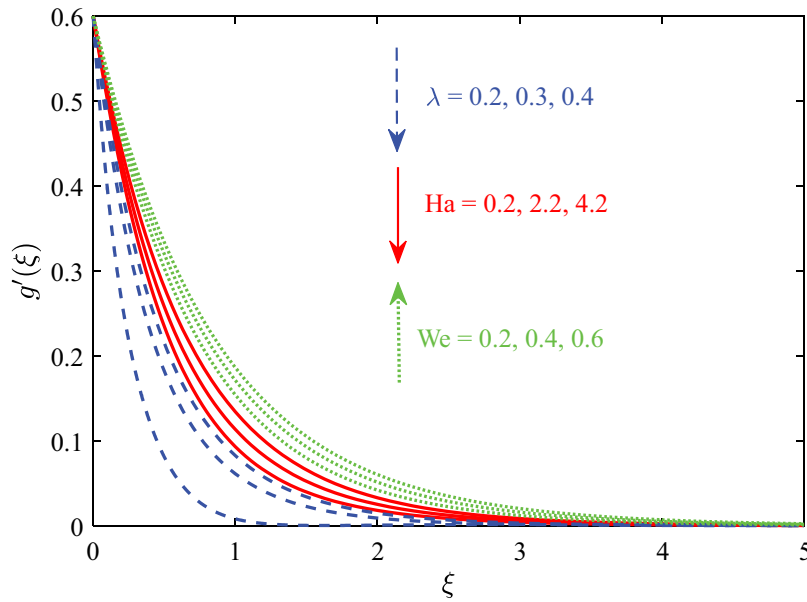


Figure 3. Velocity $g'(\xi)$ via λ , Ha and We .

more reliance on the viscosity temperatures, the Non-Newtonian liquid velocity, strong electromagnetic actuator, and heat generations are decreased.

This effect on primary and secondary velocities distributions by material dimensionless parameters connected into stretching ratio and magnetic surface electrode width impact on the Williamson flow by Figures 4 and Figures 4 and 5, as a result of this Riga plate, it assured the electro-magnetic actuators, and thus, this surface width decreased into boundary layers thickness velocities and primary flow velocities. By observing, that dragged impact on the materials was

dominated by the decreasing velocities. Anyhow, as this secondary velocity on that the flow and boundary layer thickness assured by fluid material, it happens to develop the velocity profiles is observed. As this more electromagnetic force was discussed in the secondary Williamson fluid flows, it conducts internal heat, as a result, improving this flow velocity on the wall thickness and the fluid velocities. This stretching ratio impact of Williamson flow velocity was produced in Figures 4 and 5. The reduction in the primary velocity was observed, although the increasing secondary velocity was noted. The dragging on the fluid as long as the

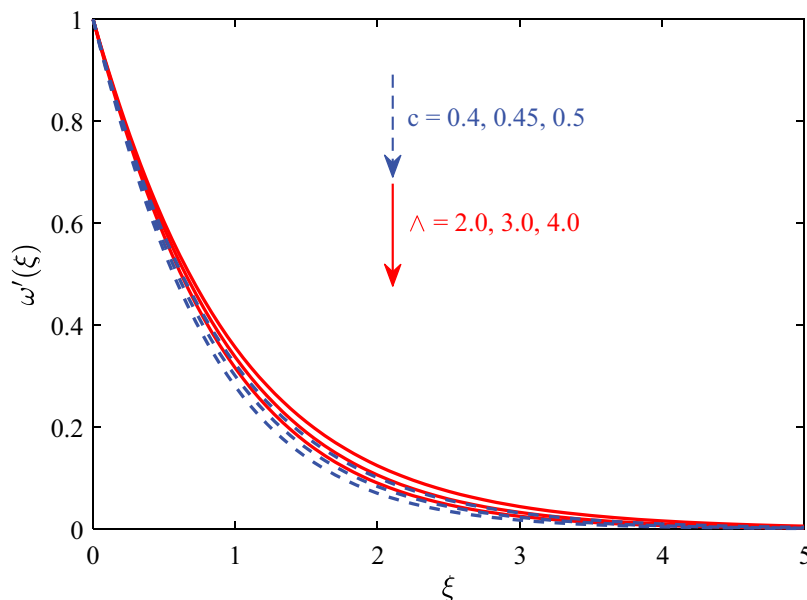


Figure 4. Velocity $\omega'(\xi)$ via λ , Ha and We .

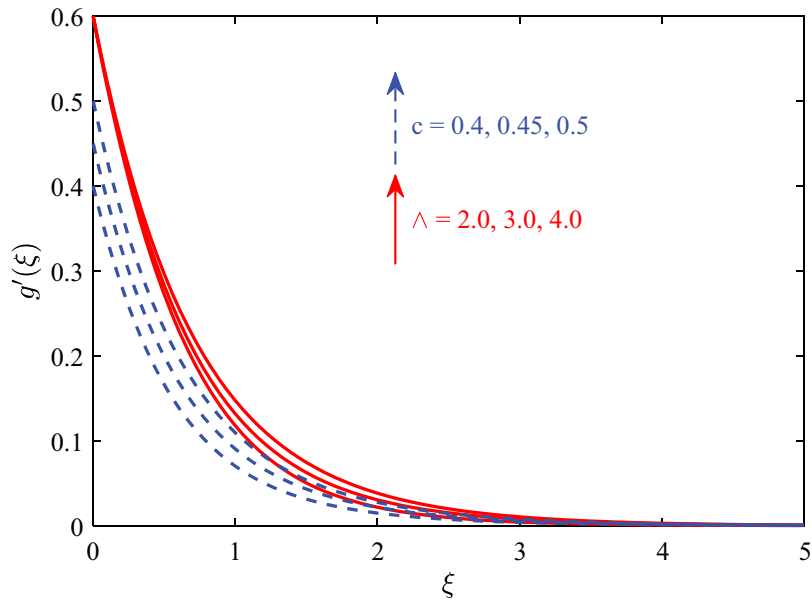


Figure 5. Velocity $g'(\xi)$ via λ , Ha and We .

horizontal Riga plate when the increasing material viscosities discouraged the heat generation and fluid particles. By that, the primary velocity was decreased by the flow stream. The secondary velocities in Figure 5 were enlarged when the wall viscosity propels internal heat. This heat produced in time breaks that molecular bond and caused the improving secondary velocities on this flow channel.

In Figure 6, the effect of the terms γ , Pr and Rd was studied on the temperature profile. By the Prandtl number raised, this flow dimensional temperature profiles. This physical performance was caused by

the declining heat boundary layer in the term of (Pr) increased. These lower boundary viscosities layers emerge on raised heat diffusions outside the system, ensuing by this decreasing temperature output. Concerning the order of RD in Figure 6, this temperature field improved. Moreover, the reaction of Williamson liquid heat distribution into the raise on γ and Rd satisfies different records by the research. Hence, the radiation and thermal conductivity had a strong effect on this material's heat conductivity. This fluid particles' heat conducting stimulated caused the temperature (re-profile into horizontal

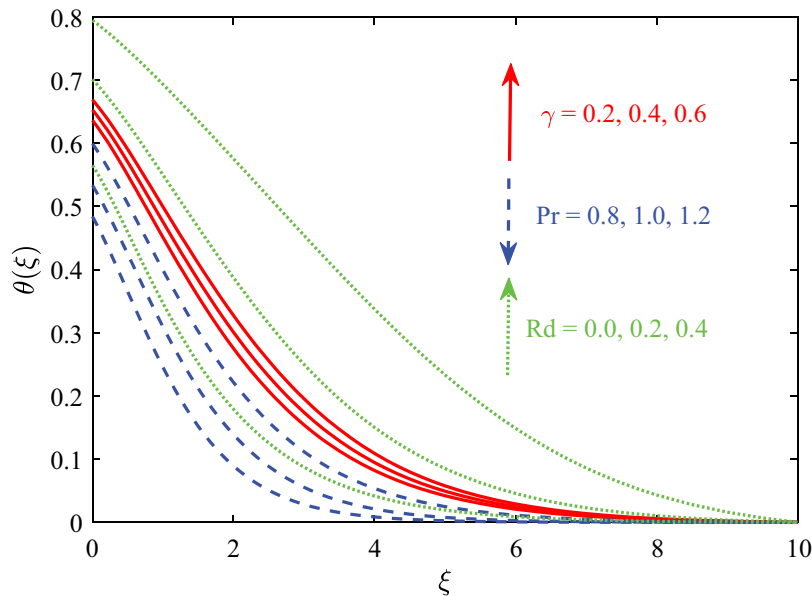


Figure 6. Velocity $\omega'(\xi)$ via λ , Ha and We .

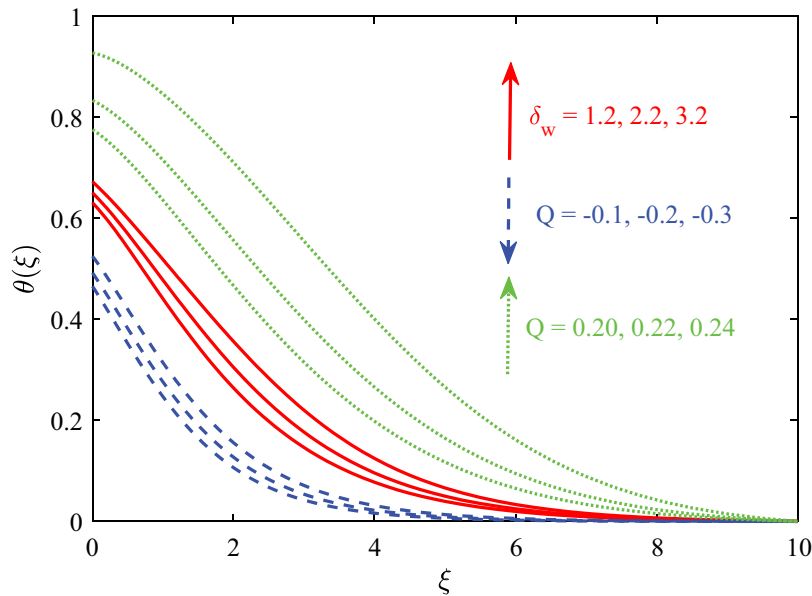


Figure 7. Velocity $\omega'(\xi)$ via λ , Ha and We .

Riga plate is rise). This radiation parameter signifies the value of thermal energies to emitting the substance in the form of photons or electromagnetic waves. This was the basic idea of the considered in the heat transport. By this radiation parameter rises, the heat transfer over the thermal radiations was advanced, resulting in greater temperatures inside this boundary layer. By the subsequent, this employing fluid experiences the rise in temperature, helped into the extension by the thermal boundary layer. These relationships among the temperature distribution and radiation parameters focused on the important act of thermal radiation by influencing heat transport and temperature profiles.

Figure 7 shows that temperature characteristics are connected to the temperature ratio parameter and heat source/sink parameters. This heat source parameter performs in the absence of the local heat input on the system, although this heat sink parameter performs the heat dissipation or extraction mechanisms. It was noted that the fact of heat source ($Q > 0$), this thermal curves for the fluid display the arising direction. The performance may clear into the case it raised heat source inside the system bringing into the greater accumulation of heat, by that ensuing in the total rise of thermal distribution by the fluid. Oppositely, this value of the heat sink parameter was the rise, and these thermal curves of the fluid display the decreasing direction. It was the case that the raised heat sinks restraint materials on the eliminated heat to the system, advancing the observable reduction in the system temperatures. These heat waves escape the system causing a decrease

in thermal energy, which changes the way temperatures are distributed. It was said that the range of heat sources in this present analysis falls within the intervals of 0–0.5. The ranges are granted in the examination by different heat input schemes and yield awareness with thermal performance in the system of distant heat source conditions.

Figure 6 also designs to enlighten the effect δ_w (as temperature ratio parameter) of the temperature distributions into the Williamson fluid materials. This Non-linear radiative effect of Williamson Fluid motions posturize displays the finding magnitude temperature field. The Radiative heat emission by that Williamson flow system could increase this thickness by the thermal boundary layers. This liquid heat and hydrodynamic is downturn the power in linked between the liquids and molecules.

Figure 8 elucidates the effect of Eckert number (Ec_1, Ec_2) and thermal Biot number Bi on temperature distribution. By graphs behave that the parameter Ec_1 and Ec_2 raised, the production of heat becomes greater by raises in temperature field and its corresponding boundary layer thickness. This Eckert number quantifies the dissipation by the kinetic energies inside the flow and is relates to a variation in enthalpy among the surrounding air and boundary layer. By this Eckert number (representing this ratio in kinetic energy by enthalpy variation) rises, this temperature variation among that wall and ambient temperatures is reduced. The reduction in temperature variation of outcomes all raised by this fluid temperature over the total domains. Subsequently, this thermal boundary layer profiles the extensions, advancing the rise of its thickness. The

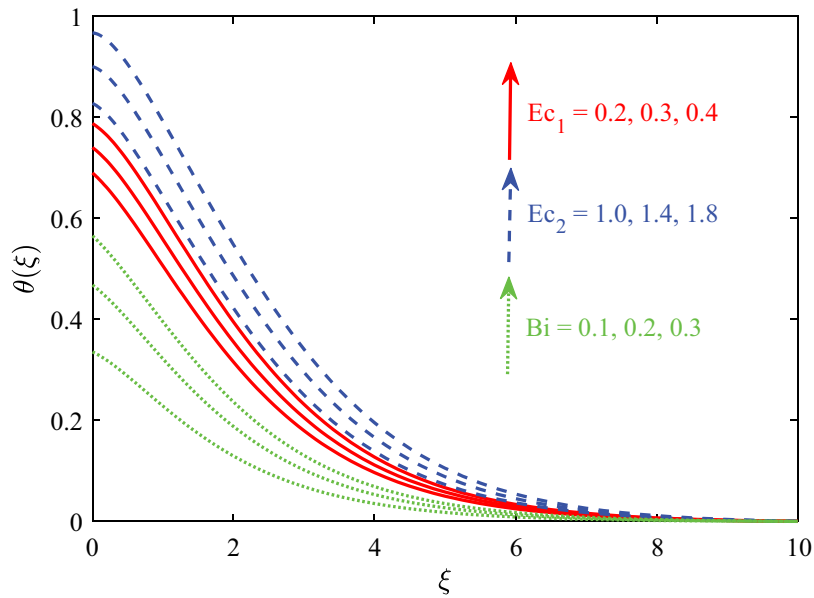


Figure 8. Velocity $\omega'(\xi)$ via λ, Ha and We .

phenomena decline the effect of viscous dissipation to the temperature distributions and consequences alter in the thermal boundary layers.

Again Figure 8 gives that effect on heat transport Biot number (Bi) for the fluid temperatures. This heat transport Biot number is characterized by the ratio of heat transport opposition on that solid-fluid intersection into internal thermal resistance inside the fluid. As the values of the heat transport Biot number increased, the temperatures of these fluids also increased. These relations are the direct consequence of interplay among the heat transport, temperature distribution, and Biot

number. The greater values of heat transport Biot number displays the strong convective heat transport, advancing the raised thermal energy changed among the fluid and its surroundings. Subsequently, these fluid temperatures experienced an increase, as illustrated in the figure.

Figure 9 illustrates the impact on the mass transfer physical factor, variable reaction terms Kr and Schmidt number (Sc), of this species diffusion rate. By Figure 9, this reaction concentration was depressed by increasing that physical term (Sc) because of thinner mass border viscosities increase mass diffusion and reduce its chemical mix rate. As a result, this Williamson

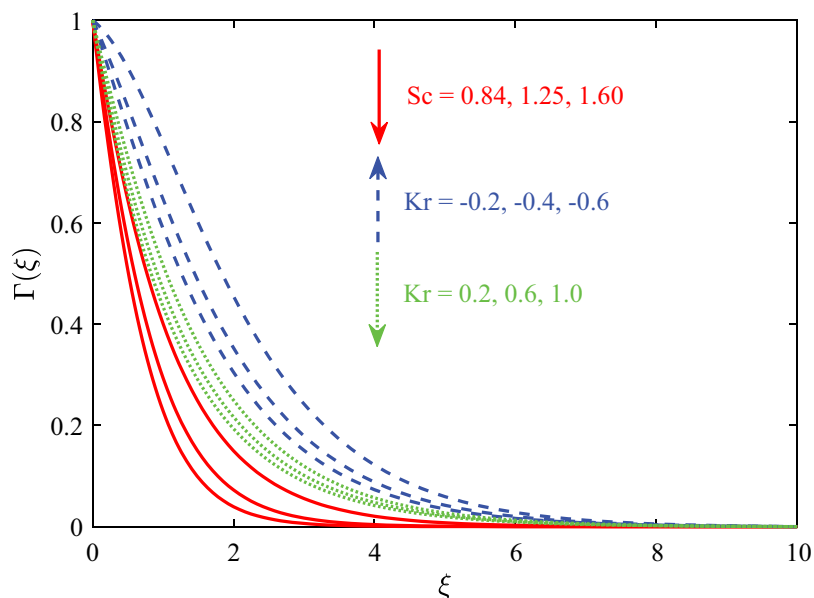


Figure 9. Velocity $\omega'(\xi)$ via λ, Ha and We .

Table 2. The numerical values of skin frictions $(Re_{x_0})^{1/2}C_{f_1}$ and $(Re_{y_0})^{1/2}C_{f_2}$.

λ	Ha	We	c	\wedge	γ	$(Re_{x_0})^{1/2}C_{f_1}$	% increase/decrease	$(Re_{y_0})^{1/2}C_{f_2}$	% increase/decrease
0.1	0.3	0.1	0.2	0.5	0.2	0.86150169	-	0.79880500	-
0.15						0.91420423	6.11752%	0.87381590	9.39039%
0.2						0.97371122	13.0249%	0.96841784	21.2333%
0.1	0.0					1.12675806	-	0.59191902	-
	0.1					1.03524831	8.12151%	0.65692756	10.9827%
	0.2					0.94733251	15.9241%	0.72531191	22.5357%
	0.3	0.0				0.87796462	-	0.80716915	-
		0.2				0.84406596	3.86105%	0.79000774	2.12612%
		0.4				0.80528994	8.27763%	0.77076777	4.50976%
		0.1	0.1			0.83073754	-	0.79135321	-
			0.3			0.88532178	6.57058%	0.84519226	6.80342%
			0.6			0.94632138	13.9134%	1.06411099	34.4673%
			0.2	0.4		0.82868819	-	0.87770144	-
				0.8		0.92197292	11.2569%	0.70363596	19.832%
				1.2		0.96680854	16.6673%	0.65703425	25.1415%
					0.0	0.86235559	-	0.79908822	-
					0.4	0.86069270	0.192831%	0.79853528	0.0691964%
					0.8	0.85920954	0.364821%	0.79803773	0.131461%

concentration diffusion reduces over the reactants on the mixture regime. Again, the variable reacting terms Kr essentially diminish the concentration outline in Figure 9 therefore the heat acquired induces a chemically reactive stopped reaction in familiar. The performance was during the less heat process; it was estimated to develop activation energy into the acquired Williamson action. This molecule link strengthened, resulting in the decreased mass transport of reactant species and, therefore, the lesser concentrated field.

Table 2 provides to notice the influence of the involved parameters of skin friction in both directions. It is noticed that skin friction along x_0 and y_0 directions

increased for incremental values of λ , c , n and opposite for Ha , We and γ . The skin friction rate of 13.02% increased along x_0 -direction and 21.23% increased along y_0 - direction when λ it increased from 0.1 to 0.2. The drag skin friction coefficient of 8.27% decreased in x_0 -direction and 4.5% decreased in y_0 -direction when c is increased from 0.1 to 0.6. Table 3 indicates that parameters Ha , Pr , Rd , δ_w , and Bi increase the Nusselt number. On the other hand, parameters λ , Ec_1 , Ec_2 , and Q reduce the Nusselt number. It is also interesting to observe from Table 3 that the Nusselt number 9.3% reduced for λ_1 and 130.56% increased for Bi . Let us consider the direction of local Sherwood numbers into

Table 3. Numerical values of heat transfer rate $(Re_{x_0})^{-1/2}Nu_{x_0}$.

λ	Ha	Pr	Ec_1	Ec_2	Rd	δ_w	Bi	Q	$(Re_{x_0})^{-1/2}Nu_{x_0}$	% increase/decrease
0.1	0.3	0.71	0.1	0.1	0.1	1.5	0.4	0.1	0.26611050	-
0.15									0.25597351	3.80932%
0.2									0.24134717	9.30566%
0.1	0.0								0.23053124	-
	0.1								0.25319202	9.82981%
	0.2								0.26269804	13.9533%
	0.3	0.5							0.21673893	-
		1.0							0.30799766	42.1054%
		1.5							0.34358415	58.5244%
		0.71	0.0						0.28333972	-
			0.2						0.24792851	12.4978%
			0.4						0.20879700	26.3086%
			0.1	0.0					0.27431851	-
				0.2					0.25767036	6.06891%
				0.4					0.24009638	12.4753%
					0.0				0.15244347	-
					0.2				0.31468653	106.428%
					0.4				0.43071928	182.544%
						1.2			0.20880153	-
						2.2			0.34366330	64.5885%
						3.2			0.57945608	177.515%
							0.1		0.08879920	-
							0.2		0.15598802	75.6638%
							0.3		0.20474069	130.566%
								-0.2	0.32561198	-
								0.0	0.28642029	12.0363%
								0.2	0.09322722	71.3686%

Table 4. Numerical values of mass transfer rate $(Re_{x0})^{-1/2}Sh_{x0}$.

λ	Ha	We	Kr	Sc	n	$(Re_{x0})^{-1/2}Sh_{x0}$	% increase/decrease
0.1	0.3	0.1	0.5	0.62	2.0	0.62830279	-
0.15						0.62132453	1.11065%
0.2						0.61260467	2.4985%
0.1	0.0					0.61739015	-
	0.1					0.62406940	1.08185%
	0.2					0.62739975	1.62128%
	0.3	0.0				0.63031234	-
		0.2				0.62609221	0.66953%
		0.4				0.62079965	1.5092%
		0.1	-0.4			0.14816137	-
			0.0			0.42791593	188.817%
			0.4			0.59329279	300.437%
				0.5		0.55402581	-
				1.0		0.82979411	49.7754%
				1.5		1.04955532	89.4416%
					1.0	0.72451003	-
					2.0	0.62792520	13.3311%
					3.0	0.57969542	19.9879%

differences on distant parameters such as λ , Ha , We , Kr , Sc and n . From this reason, Table 4 displays that the difference in the Sherwood number increases with Ha and Kr , while it decreases with λ , We , Sc , and n . the maximum increase rate of the Sherwood number, i.e. 300.43%, is observed for increasing values of the chemical reaction parameters.

6. Conclusions

The major concern of this study is to work the radiative reactive Williamson fluid by the Riga plate in the presence of variable material viscosity into advanced features on binary chemical reaction and nonlinear thermal radiation. Furthermore, these simulations on convective boundary restraints by temperature distribution were enforced on the attributes flow situations. The physical aspect of the investigation was captured by different physical constants. The following results were recorded from the current study.

- (1) This escalating profile on primary velocity had been observed by developing values of Hartman number and opposite behavior is noted for viscosity parameter and stretching ratio.
- (2) The viscosity parameter and Hartman number declined the secondary velocity of Williamson fluid efficiency and the rest of the parameters i.e. stretching ratio and electrode width are uplifted.
- (3) Due to variations in the thermal conductivity factor, radiation parameter, and the temperature distribution, temperature ratio hikes up.

- (4) The addition of chemical reactions to liquid fluctuations reduced the concentration of the total liquid stretch. Again, the rise in Schmidt's number means a reduction in mass diffusivity leading to a downturn the fluid concentrations.
- (5) It was alluring to observe the heavier species were positive in advance of the Sherwood number and the reaction rate was negative in advance of the Sherwood number.
- (6) Nusselt number gets higher for Biot number it is 177.51%, and in the absence of thermal radiation, it was 182.54%. Therefore higher heat transfer rate is observed for thermal radiation.
- (7) Temperature distribution declines for higher estimation of Prandtl number and heat absorption.

The results of the discovery can use the technology and industry improperly taken into their employing fluids to enhance productivity. Thus, further analysis was suggested into this concentric cylinder flow over the Riga plate and slip conditions.

Acknowledgments

Authors are thankful to the reviewers and editor for their useful suggestions which were really helping for the improvement of the manuscript.

Disclosure statement

No potential conflict of interest was reported by the author(s).

Notes on contributors

Dr. Kotha Gangadhar is an Associate Professor in the department of Mathematics at Acharya Nagarjuna University, Andhra Pradesh State, India. He earned his Ph.D. in Fluid Dynamics from Sri Venkateswara University, Andhra Pradesh State, India in 2009. His research interest includes MHD, nanofluid flows over stretching surface and heat and mass transfer of non-Newtonian/Newtonian fluids. He has authored and co-authored over 103 publications in archival international journals and conferences. His current h-index is 19 and total citations are 1246

T. Sujana Sree working as assistant professor in mathematics, RVR & JC College of Engineering, Gunture. She 3 papers in reputed journals.

Prof. Ali J. Chamkha is a Distinguished Professor of Mechanical Engineering and Dean of Engineering at Kuwait College of Science and Technology. He earned his Ph.D. in Mechanical Engineering from Tennessee Technological University, USA, in 1989. His research interests include multi-phase fluid-particle dynamics, nanofluids dynamics, fluid flow in porous media, heat and mass transfer, magneto hydrodynamics and fluid-particle separation. He has authored and co-authored over 1200 publications in archival international journals and conferences. His current h-index is 130 and total citations are 53,924.

ORCID

Kotha Gangadhar  <http://orcid.org/0000-0002-0264-2512>

T. Sujana Sree  <http://orcid.org/0009-0006-6316-2703>

Ali J. Chamkha  <http://orcid.org/0000-0002-8335-3121>

References

- [1] Gailitis A, Lielausis O. On a possibility to reduce the hydrodynamic resistance of a plate in an electrolyte. *Appl Magnetohydrodynamics Rep Phys Inst Riga*. 1961;12:143–146.
- [2] Grinberg E. On determination of properties of some potential fields. *Appl Magnetohydrodynamics Rep Phys Inst Riga*. 1961;12:147–154.
- [3] Asogwa KK, Kumar KT, Goud BS, et al. Significance of nanoparticle shape factor and buoyancy effects on a parabolic motion of EMHD convective nanofluid past a Riga plate with ramped wall temperature. *Eur Phys J Plus*. 2023;138(6):572. doi: 10.1140/epjp/s13360-023-04170-3
- [4] Ali B, Jubair S. Motile microorganism-based ternary nanofluid flow with the significance of slip condition and magnetic effect over a Riga plate. *J Therm Anal Calorim*. 2023;148(20):11203–11213. doi: 10.1007/s10973-023-12397-6
- [5] Kayikci S, Eswaramoorthi S, Postalcioğlu S, et al. Thermal analysis of radiative water- and glycerin-based carbon nanotubes past a Riga plate with stratification and non-fourier heat flux theory. *J Therm Anal Calorim*. 2023;148(2):533–549. doi: 10.1007/s10973-022-11669-x
- [6] Nagaraja L, Reddy MS, Reddy MS. Heat transfer of non-newtonian Williamson fluid flow past a circular cylinder with suction and injection. *Int J Innov Res Sci Eng Tech*. 2017;6:48–54.
- [7] Rao AS, Amanullah CH, Nagendra N, et al. Hydromagnetic flow and heat transfer in a williamson non-newtonian fluid from a horizontal circular cylinder with newtonian heating. *Int J Appl Comput Math*. 2017;3(4):3389–3409. doi: 10.1007/s40819-017-0304-x
- [8] Abualnaja KH. Homotopy perturbation method for MHD non-newtonian Williamson fluid over exponentially stretching sheet with viscous dissipation and convective boundary condition. *Int J Mod Phys C*. 2019;30(11):1950088. doi: 10.1142/S0129183119500888
- [9] Sharma RP, Thumma T, Mishra SR, et al. Cross-diffusion of magnetohydrodynamic Williamson and Casson fluid flow past a slendering horizontal surface with variable thickness and multi-slip conditions: an implicit finite difference approach. *Eur Phys J Plus*. 2023;138(10):875. doi: 10.1140/epjp/s13360-023-04487-z
- [10] Patil VS, Humane PP, Patil AB. MHD williamson nanofluid flow past a permeable stretching sheet with thermal radiation and chemical reaction. *Int J Model Simulat*. 2023;43(3):185–199. doi: 10.1080/02286203.2022.2062166
- [11] Nazeer M, Ramesh K, Farooq H, et al. Impact of gold and silver nanoparticles in highly viscous flows with different body forces. *Int J Model Simulat*. 2023;43(4):376–392. doi: 10.1080/02286203.2022.2084217
- [12] Mukhopadhyay S. Effect of radiation and variable fluid viscosity on flow and heat transfer along a symmetric wedge. *J Appl Fluid Mech*. 2009;2(2):29–34.
- [13] Akolade MT, Olabode JO, Tijani YO, et al. Bioconvection in eyring–Powell fluid with composite features of variable viscosity and motile microorganism density. *Eur Phys J Plus*. 2023;138(8):736. doi: 10.1140/epjp/s13360-023-04361-y
- [14] Chaurasiya V, Chaudhary RK, Awad MM, et al. A numerical study of a moving boundary problem with variable thermal conductivity and temperature-dependent moving PCM under periodic boundary condition. *Eur Phys J Plus*. 2022;137(6):714. doi: 10.1140/epjp/s13360-022-02927-w
- [15] Vaidya H, Choudhari R, Baleanu D, et al. On electro-osmosis in peristaltic blood flow of magnetohydrodynamics carreau material with slip and variable material characteristics. *Int J Modern Phys B*. 2023;37(4):2350032. doi: 10.1142/S0217979223500327
- [16] Ramzan M, Shaheen N, Ghazwani HAS, et al. Impact of higher-order chemical reaction with generalized Fourier and Fick law on a maxwell nanofluid flow past a rotating cone with variable thermal conductivity. *Int J Modern Phys B*. 2023;37(7):2350062. doi: 10.1142/S0217979223500625
- [17] Vijay N, Sharma K. Entropy generation analysis in MHD hybrid nanofluid flow: effect of thermal radiation and chemical reaction. *Numerical Heat Transfer Part B: Fundamentals*. 2023;84(1):66–82. doi: 10.1080/10407790.2023.2186989
- [18] Ejaz I, Mustafa M. A comparative study of different viscosity models for unsteady flow over a decelerating

- rotating disk with variable physical properties. *Int J Heat Mass Transf.* **2022**;135:106155. doi: [10.1016/j.icheatmasstransfer.2022.106155](https://doi.org/10.1016/j.icheatmasstransfer.2022.106155)
- [19] Kumawat C, Sharma BK, Al-Mdallal QM, et al. Entropy generation for MHD two phase blood flow through a curved permeable artery having variable viscosity with heat and mass transfer. *Int J Heat Mass Transf.* **2022**;133:105954. doi: [10.1016/j.icheatmasstransfer.2022.105954](https://doi.org/10.1016/j.icheatmasstransfer.2022.105954)
- [20] Hussain A, Farooq N. Gyrotactic micro-organisms swimming under the hyperbolic tangent blood nano material and solar biomimetic system over the esophagus. *Int J Heat Mass Transf.* **2023**;141:106579. doi: [10.1016/j.icheatmasstransfer.2022.106579](https://doi.org/10.1016/j.icheatmasstransfer.2022.106579)
- [21] Aziz A, Aziz A, Ullah I, et al. Numerical simulation for 3D rotating flow of nanofluid with entropy generation. *Int J Model Simulat.* **2023**;43(3):101–122. doi: [10.1080/02286203.2022.2051993](https://doi.org/10.1080/02286203.2022.2051993)
- [22] Bhatti MM, Sait SM, Ellahi R, et al. Thermal analysis and entropy generation of magnetic eyring-powell nanofluid with viscous dissipation in a wavy asymmetric channel. *Int J Numer Methods Heat Fluid Flow.* **2023**;33(5):1609–1636. doi: [10.1108/HFF-07-2022-0420](https://doi.org/10.1108/HFF-07-2022-0420)
- [23] Naseem T, Shahzad A. Thermal transport in nanofluid across a radiated permeable sheet with irreversible effects based on the shape of the particles. *Int J Numer Methods Heat Fluid Flow.* **2023**;33(6):2073–2099. doi: [10.1108/HFF-10-2022-0593](https://doi.org/10.1108/HFF-10-2022-0593)
- [24] Gangadhar K, Shashidhar Reddy K, Wakif A. Wall jet plasma fluid flow problem for hybrid nanofluids with joule heating. *Int J Ambient Energy.* **2023**;44(1):2459–2468. doi: [10.1080/01430750.2023.2251482](https://doi.org/10.1080/01430750.2023.2251482)
- [25] Mahmud K, Rana S, Al-Zubaidi A, et al. Interaction of Lorentz force with cross swimming microbes in couple stress nano fluid past a porous Riga plate. *Int J Heat Mass Transf.* **2022**;138:106347. doi: [10.1016/j.icheatmasstransfer.2022.106347](https://doi.org/10.1016/j.icheatmasstransfer.2022.106347)
- [26] Juhany KA, Shahzad F, Alzhrani S, et al. Finite element mechanism and quadratic regression of magnetized mixed convective burgers' nanofluid flow with applying entropy generation along the riga surface. *Int J Heat Mass Transf.* **2023**;142:106631. doi: [10.1016/j.icheatmasstransfer.2023.106631](https://doi.org/10.1016/j.icheatmasstransfer.2023.106631)
- [27] Farooq M, Walie MH, Ahmad S, et al. Assessment of squeezing phenomenon in non-linear stratified fluid flow with slip conditions through Darcy porous material. *Int J Heat Mass Transf.* **2023**;146:106945. doi: [10.1016/j.icheatmasstransfer.2023.106945](https://doi.org/10.1016/j.icheatmasstransfer.2023.106945)
- [28] Shafiq A, Çolak AB, Sindhu TN. Significance of EMHD graphene oxide (GO) water ethylene glycol nanofluid flow in a darcy-forchheimer medium by machine learning algorithm. *Eur Phys J Plus.* **2023**;138(3):213. doi: [10.1140/epjp/s13360-023-03798-5](https://doi.org/10.1140/epjp/s13360-023-03798-5)
- [29] Shoaib M, Naz S, Nisar KS, et al. MHD casson nanofluid in darcy-forchheimer porous medium in the presence of heat source and arrhenious activation Energy: applications of neural networks. *Int J Model Simulat.* **2023**;43(4):438–461. doi: [10.1080/02286203.2022.2091973](https://doi.org/10.1080/02286203.2022.2091973)
- [30] He J-H, Elgazery NS, Abd Elazem NY. Magneto-radiative gas near an unsmooth boundary with variable temperature. *Int J Numer Methods Heat Fluid Flow.* **2023**;33(2):545–569. doi: [10.1108/HFF-05-2022-0285](https://doi.org/10.1108/HFF-05-2022-0285)
- [31] Fang J, Wang M, Yue J, et al. Dual-polarization strong nonreciprocal thermal radiation under near-normal incidence. *Int J Heat Mass Transf.* **2023**;148:107031. doi: [10.1016/j.icheatmasstransfer.2023.107031](https://doi.org/10.1016/j.icheatmasstransfer.2023.107031)
- [32] Padma Devi M, Srinivas S. Two layered immiscible flow of viscoelastic liquid in a vertical porous channel with hall current, thermal radiation and chemical reaction. *Int J Heat Mass Transf.* **2023**;142:106612. doi: [10.1016/j.icheatmasstransfer.2023.106612](https://doi.org/10.1016/j.icheatmasstransfer.2023.106612)
- [33] Mahabaleshwar US, Sneha KN, Pérez LM, et al. An unsteady flow through porous media leads to a newtonian fluid presence of CNTS and suction/injection. *Int J Heat Mass Transf.* **2023**;145:106844. doi: [10.1016/j.icheatmasstransfer.2023.106844](https://doi.org/10.1016/j.icheatmasstransfer.2023.106844)
- [34] Shamshuddin MD, Salawu SO, Shahzad F, et al. Thermal examination of chemical interaction and thermophoretic diffusion of Williamson fluid flow across riga plate surface with nonlinearity radiation flux. *Numer Heat Transfer.* **2023**:1–15. Part A: Applications. doi:[10.1080/10407782.2023.2251092](https://doi.org/10.1080/10407782.2023.2251092).
- [35] Qureshi MA. Thermal capability and entropy optimization for prandtl-eyring hybrid nanofluid flow in solar aircraft implementation. *Alex Eng J.* **2022**;61(7):5295–5307. doi: [10.1016/j.aej.2021.10.051](https://doi.org/10.1016/j.aej.2021.10.051)
- [36] Srinivas RC, Naikoti K, Rashidi MM. MHD flow and heat transfer characteristics of Williamson nanofluid over a stretching sheet with variable thickness and variable thermal conductivity. *Trans A Razmadze Math Inst.* **2017**;171(2):195–211. doi: [10.1016/j.trmi.2017.02.004](https://doi.org/10.1016/j.trmi.2017.02.004)
- [37] Dada MS, Onwubuoya C. Variable viscosity and thermal conductivity effects on Williamson fluid flow over a slandering stretching sheet. *WJE.* **2020**;17(3):357–371. doi: [10.1108/WJE-08-2019-0222](https://doi.org/10.1108/WJE-08-2019-0222)
- [38] Akbar S, Sohail M. Three dimensional MHD viscous flow under the influence of thermal radiation and viscous dissipation. *IJEMD-M.* **2022**;1(3):106–117. doi: [10.54938/ijemdm.2022.01.3.122](https://doi.org/10.54938/ijemdm.2022.01.3.122)
- [39] Li S, Akbar S, Sohail M, et al. Influence of buoyancy and viscous dissipation effects on 3D magneto hydrodynamic viscous hybrid nano fluid (MgO– TiO₂) under slip conditions. *Case Stud Thermal Eng.* **2023**;49:103281. doi: [10.1016/j.csite.2023.103281](https://doi.org/10.1016/j.csite.2023.103281)
- [40] Nazir U, Sohail M, Mukdasai K, et al. Applications of variable thermal properties in Carreau material with ion slip and hall forces towards cone using a non-fourier approach via FE-method and mesh-free study. *Front Mater.* **2022**;9:1054138. doi: [10.3389/fmats.2022.1054138](https://doi.org/10.3389/fmats.2022.1054138)
- [41] Imran N, Javed M, Sohail M, et al. Multi-objective study using entropy generation for Ellis fluid with slip conditions in a flexible channel. *Int J Modern Phys B.* **2023**;37(27):2350316. doi: [10.1142/S0217979223503162](https://doi.org/10.1142/S0217979223503162)
- [42] Liu J, Nazir U, Sohail M, et al. Numerical investigation of thermal enhancement using MoS₂-Ag/C₂H₆O₂ in prandtl fluid with soret and Dufour effects across a vertical sheet. *AIP Adv.* **2023**;13(7):075112. doi: [10.1063/5.0152262](https://doi.org/10.1063/5.0152262)

- [43] Khan RM, Imran N, Mehmood Z, et al. A Petrov–galerkin finite element approach for the unsteady boundary layer upper-convected rotating maxwell fluid flow and heat transfer analysis. *Waves Rand Complex Media*. 2022;1–18. doi: [10.1080/17455030.2022.2055201](https://doi.org/10.1080/17455030.2022.2055201)
- [44] Khan RM, Ashraf W, Sohail M, et al. On behavioral response of microstructural slip on the development of magnetohydrodynamic micropolar boundary layer flow. *Complexity*. 2020;2020:8885749. doi: [10.1155/2020/8885749](https://doi.org/10.1155/2020/8885749)
- [45] Hayat T, Muhammad T, Alsaedi A, et al. Three-dimensional flow of nanofluid with Cattaneo–Christov double diffusion. *Results Phys*. 2016;6:897–903. doi: [10.1016/j.rinp.2016.10.017](https://doi.org/10.1016/j.rinp.2016.10.017)
- [46] Sohail M, Nazir U, Naz S, et al. Utilization of galerkin finite element strategy to investigate comparison performance among two hybrid nanofluid models. *Sci Rep*. 2022;12(1):18970. doi: [10.1038/s41598-022-22571-9](https://doi.org/10.1038/s41598-022-22571-9)
- [47] Sohail M, Nazir U. Numerical computation of thermal and mass transportation in williamson material utilizing modified fluxes via optimal homotopy analysis procedure, waves in random and complex media. 2023. doi: [10.1080/17455030.2023.2226230](https://doi.org/10.1080/17455030.2023.2226230)
- [48] Abouelregal AE, Zakaria K, Sirwah MA, et al. Viscoelastic initially stressed microbeam heated by an intense pulse laser via photo-thermoelasticity with two-phase lag. *International J Modern Physics C*. 2022;33(6):2250073. doi: [10.1142/S0129183122500735](https://doi.org/10.1142/S0129183122500735)
- [49] Abouelregal AE, Ahmad H, Elagan SK, et al. Modified moore-gibson-thompson photo-thermoelastic model for a rotating semiconductor half-space subjected to a magnetic field. *International J Modern Physics C*. 2021;32(12):2150163. doi: [10.1142/S0129183121501631](https://doi.org/10.1142/S0129183121501631)
- [50] Abouelregal AE, Ahmad H, Badr SK, et al. Thermo-viscoelastic behavior in an infinitely thin orthotropic hollow cylinder with variable properties under the non-Fourier MGT thermoelastic model. *Z Angew Math Mech*. 2022;102(1):e202000344. doi: [10.1002/zamm.202000344](https://doi.org/10.1002/zamm.202000344)
- [51] Abouelregal AE, Ahmad H, Badr SK, et al. Viscoelastic stressed microbeam analysis based on moore-gibson-thompson heat equation and laser excitation resting on Winkler foundation. *J Low Frequency Noise Vib Active Control*. 2022;41(1):118–139. doi: [10.1177/14613484211040318](https://doi.org/10.1177/14613484211040318)
- [52] Abouelregal AE, Moustapha MV, Nofal TA, et al. Generalized thermoelasticity based on higher-order memory-dependent derivative with time delay. *Results Phys*. 2021;20:103705. doi: [10.1016/j.rinp.2020.103705](https://doi.org/10.1016/j.rinp.2020.103705)